ECS Transactions, 35 (14) 39-51 (2011)
10.1149/1.3644902 ©The Electrochemical Society

Computer Modeling of Crystalline Electrolytes – Lithium Thiophosphates and Phosphates

N. D. Lepley and N. A. W. Holzwarth

Department of Physics, Wake Forest University, Winston-Salem, NC 27109, USA

First principles modeling techniques are used to examine the stabilities, structures, and Li ion migration properties of (thio)phosphate electrolyte materials, focusing on the "superionic" electrolyte $Li_7P_3S_{11}$. We report on our progress toward understanding both vacancy and interstitial mechanisms for Li ion migration.

I. Introduction

During the last 5 years, lithium thiophosphate solid electrolyte materials have been developed[1, 2, 3, 4, 5] for use in all-solid-state rechargeable batteries. In particular, crystalline $Li_7P_3S_{11}$ has been characterized as a superionic conducting material[2, 3, 4, 5] possessing room temperature conductivities as high as 10^{-3} S/cm, which is 1000 times greater than that of the commercial solid electrolyte material LiPON.[6] Building on our previous work,[7] we report on computer modeling studies of this material as well as those of related phosphates. We present results on meta-stable crystal structures, formation energies, and mechanisms of Li ion migration.

Section II summarizes the computational methods and their validation. Section III presents computed heats of formation of several (thio)phosphate materials and discusses their relative stabilities. Section IV focuses on Li ion migration in $Li_7P_3S_{11}$, including some results on energy barriers for Li ion vacancy migration and the identification of several interstitial sites expected to be important for interstitial migration. Section V contains the summary and discussion of this paper.

II. Computational methods

The calculational methods are based on density functional theory.[8, 9] The calculations were carried out using the Quantum Espresso (*pwscf*)[10] and *abinit*[11] packages. Estimates of the migration energies E_m for the Li ion diffusion were calculated using the nudged elastic band (NEB) method[12, 13, 14] as implemented in the *pwscf* code. Visualizations were constructed using the *OpenDX*[15] and *XCrySDEN*[16] software packages.

Further details regarding the computational methods are described in our previous work.[7, 17] In the present work, the majority of the results were obtained using ultra-soft pseudopotentials (USPP)[18] and the *pwscf* code. In order to quantify numerical errors due to pseudopotential generation, we also performed some of the calculations using the projector augmented wave (PAW)[19] formalism. The basis and projector functions for this formalism were generated by the *atompaw*[20] code and used in both the *abinit* and *pwscf* packages.

For analyzing formation energies and other perfect crystal properties, all calculations were performed with plane wave expansions of the wavefunction including $|\mathbf{k}+\mathbf{G}|^2 \leq 64$ bohr^{-2} and relatively dense sampling of the Brillouin zone. For example, crystals of $Li_7P_3S_{11}$ were calculated with a Monkhorst-Pack[21] $\mathbf{k}$-point sampling of $3 \times 6 \times 3$. For analyzing Li ion migration in $Li_7P_3S_{11}$, a fixed volume supercell of $1 \times 2 \times 1$ units was constructed. This choice of supercell is approximately isotropic and remains a computationally manageable size – 84 atoms. Since only relative energies are important for this part of the study, less stringent convergence parameters could be used – namely – $|\mathbf{k}+\mathbf{G}|^2 \leq 32$ bohr^{-2} and a single $\mathbf{k}$-point sampling of the Brillouin zone.

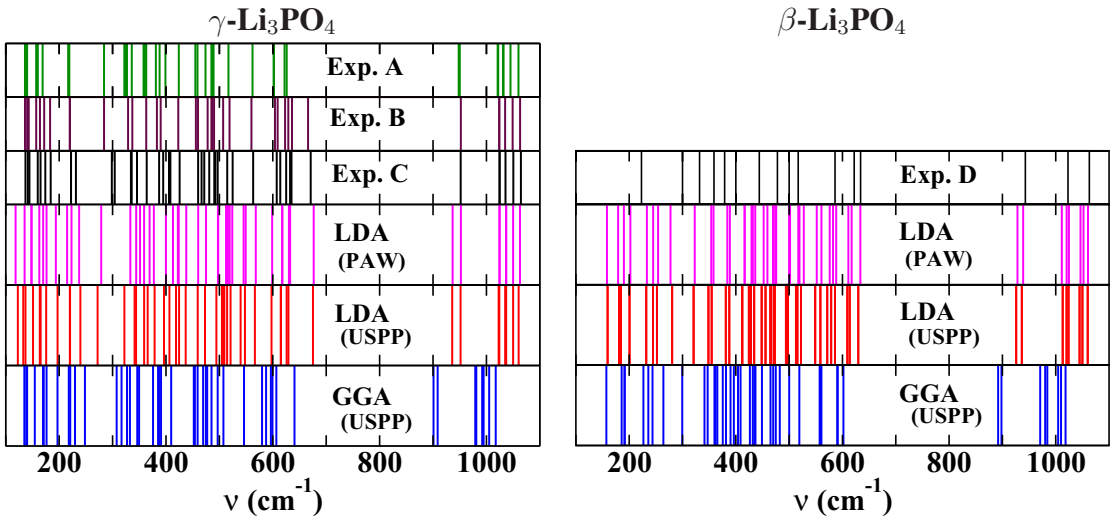

FIG. 1: Comparison of experimental and calculated Raman spectra for γ-Li_3PO_4 (left) and β-Li_3PO_4 (right). The experimental references are A: (Ref.[22] at room temperature), B: (Ref.[23] at room temperature), C: (Ref.[23] at liquid nitrogen temperature), and D: (Ref. [24] measured at liquid nitrogen temperature). These are compared with calculated results using PAW and USPP formalisms and LDA and GGA exchange-correlation functionals.

In order for computer simulations, such as those reported here, to make useful contributions, it is important that the results be validated with respect to experiment. This issue was addressed in our previous work[25] in terms of the comparison of calculated and measured Raman active vibrational frequencies of Li_3PO_4. Li_3PO_4 is one of the few related materials for which high precision measurements that probe the energy surface are available.[23, 24, 22] Figure 1 updates the calculated results obtained using two different

exchange-correlation functionals: the local density approximation (LDA)[26] and the generalized gradient approximation (GGA)[27] as compared with the experimental spectra. Results obtained by using both the PAW and USPP formalisms with the LDA exchange-correlation functional are compared. From this figure, we see that for high frequency vibrations, ($\nu > 600\,\mathrm{cm}^{-1}$) the differences between both of the LDA calculations and experiment are minimal. For lower frequency vibrations, noticeable differences between the two LDA calculations appear and all of the results differ significantly from experiment, suggesting that the results are numerically unreliable in this range. This is not surprising because the phonon calculation involves computing second order derivatives of the energy functions. Since we expect that our relative energies are approximated with an accuracy within 0.1 eV, the energy derivatives become much less reliable at low frequency. These results reinforce our previous conclusions that LDA exchange-correlation functional calculations can provide a reliable modeling tool for investigating this class of electrolyte materials. On the other hand, in the two examples shown in Fig. 1, the GGA results are significantly different from experiment at all frequencies.

III. Heats of Formation

The results of density functional calculations include the ground state energy per unit cell, obtained with variational accuracy. Therefore, we expect the heats of formation of these materials to be well approximated. We have calculated the heats of formation for many of the Li (thio)phosphates and related materials as presented in Table I. The standard state reference energies were obtained in the same way as described in our earlier work (Ref. [7, 17]). The present results obtained using the ultra-soft pseudopotential scheme (labeled "USPP") differ slightly from the earlier work. This is due to more stringent convergence parameters and a slight readjustment of the standard energy of O on the basis of additional calorimetry data[28] for Li_2O_2, SO_3, and Li_2SO_4 using the structural determinations of references [29], [30] and [31], respectively. Comparing the present results with those of the previous work as well as comparing the USPP with the PAW results in the current calculations show that the mathematical errors of the method are well within 0.1 eV/formula unit. The comparison of all of the calculated results with experimental measurements show a deviation of up to 0.4 eV/formula unit.

The negative heats of formation listed in Table I affirm that all of the materials listed are stable with respect to decomposition to the elements in their standard states. However, not all of the materials calculated have been observed. For example, as reported in our earlier work [7], $Li_4P_2S_6$ has been observed[33] but $Li_4P_2S_7$ has only been mentioned as having a glassy form.[34] Correspondingly, our calculations predict $Li_4P_2S_6$ to be more stable than $Li_4P_2S_7$ in the sense that

$$\Delta H(\mathrm{Li_4P_2S_6}) - (\Delta H(\mathrm{Li_4P_2S_7}) - \Delta H(\mathrm{S})) = -0.8\ \mathrm{eV}. \quad (1)$$

On the other hand $Li_4P_2O_7$ has been well characterized[35], but we have not found $Li_4P_2O_6$ mentioned in the literature. Our calculations find $Li_4P_2O_7$ to be substantially more stable

TABLE I: Heats of formation ΔH (eV per formula unit) calculated for the lithium (thio)phosphate and related materials, comparing calculated USPP and PAW results and experimental measurements[28] when available. Also listed are the structures assumed for the calculations, described in terms of the space group using the notation of Ref. [32].

		ΔH (eV per formula unit)		
Material	Structure	(USPP)	(PAW)	EXP
Li_2O	$Fm\bar{3}m$ (#225)	-6.18	-6.19	-6.20
Li_2O_2	$P6_3/mmc$ (#194)	-6.54	-6.53	-6.57
β-Li_3PO_4	$Pmn2_1$ (#31)	-21.41	-21.40	
γ-Li_3PO_4	$Pnma$ (#62)	-21.38	-21.37	-21.72
$Li_4P_2O_6$	$P\bar{3}1m$ (#162)	-30.03	-29.93	
$Li_4P_2O_7$	$P\bar{1}$ (#2)	-34.26	-34.21	
$Li_7P_3O_{11}$	$P\bar{1}$ (#2)	-55.32	-55.26	
Li_2S	$Fm\bar{3}m$ (#225)	-4.29	-4.30	-4.57
Li_2S_2	$P6_3/mmc$ (#194)	-4.09	-4.10	
β-Li_3PS_4	$Pmn2_1$ (#31)	-8.36	-8.35	
γ-Li_3PS_4	$Pnma$ (#62)	-8.17	-8.16	
$Li_4P_2S_6$	$P\bar{3}1m$ (#162)	-12.41	-12.38	
$Li_4P_2S_7$	$P\bar{1}$ (#2)	-11.58	-11.54	
$Li_7P_3S_{11}$	$P\bar{1}$ (#2)	-20.00	-19.95	
SO_3	$Pna2_1$ (#33)	-4.83	-4.86	-4.71
Li_2SO_4	$P2_1/a$ (#14)	-14.74	-14.76	-14.89

than $Li_4P_2O_6$ in the sense that

$$\Delta H(Li_4P_2O_7) - (\Delta H(Li_4P_2O_6) + \tfrac{1}{2}\Delta H(O_2)) = -4.3\ \text{eV}. \quad (2)$$

In this work, we focus on the ceramic material $Li_7P_3S_{11}$. Its crystal structure has been determined by X-ray analysis[2] and also neutron diffraction[36] to be triclinic with a center of inversion ($P\bar{1}$). Figure 2 shows a diagram of our optimized structure of this material along with its phosphate analog. For ease in visualization, the origin of the crystal is shifted by $\frac{1}{2}\mathbf{b}$. From the given viewpoint (along the $\mathbf{b}$ axis), it is apparent that both structures are characterized by well-packed arrangements of (thio)phosphate dimers – ($Li_4P_2S_4$) $Li_4P_2O_4$ – and monomers – (Li_3PS_4) Li_3PO_4.

Our structural relaxation study finds $Li_7P_3S_{11}$ to have at least two meta stable phases. The lowest energy structure that we found was obtained by optimizing the lattice parameters and fractional coordinates determined from X-ray powder diffraction.[2] The lattice parameters of this lowest energy configuration of $Li_7P_3S_{11}$ are given in Table II, which compares the experimental results with the calculated USPP and PAW results. The USPP and PAW results are in very close agreement with each other. The calculations underestimate the lattice constants along the $\mathbf{a}$ and $\mathbf{c}$ axes, as expected for LDA calculations, while they

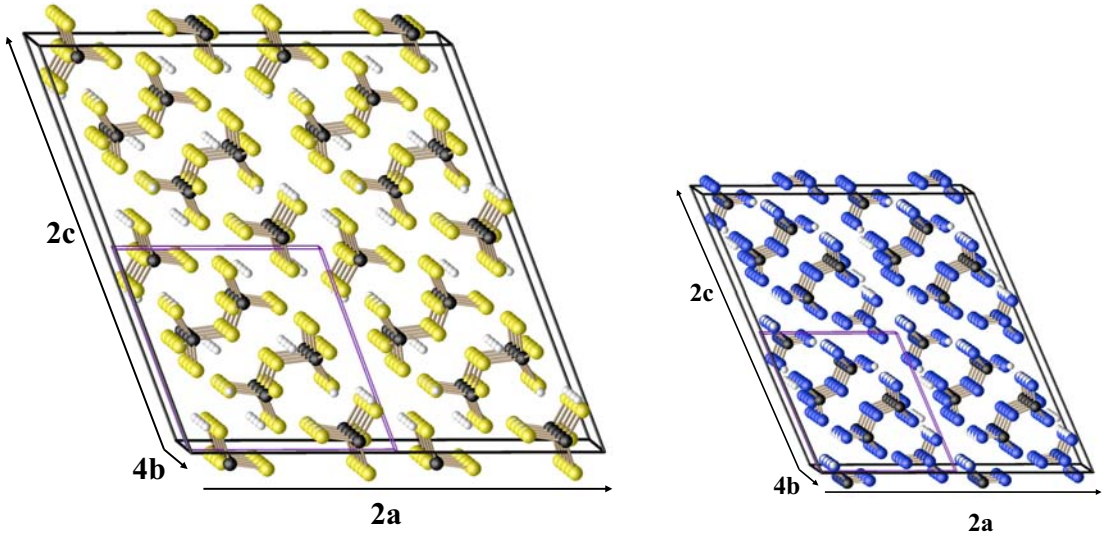

FIG. 2: Ball and stick model of optimized structures of $Li_7P_3S_{11}$ (left) and $Li_7P_3O_{11}$ (right). The thick bar lines indicate the boundaries of the multicell diagram and the thin bar lines indicate the boundaries of the primitive unit cell. The thiophosphate groups are designated with bonded yellow (S) and black (P) spheres. The phosphate groups are designated with bonded blue (O) and black (P) spheres.

overestimate the lattice constant along the b axis. By starting from the initial configuration based on neutron powder diffraction,[36] we obtained a different meta-stable structure having an energy 0.1 eV higher. Understanding the details of this metastable phase is the subject of ongoing work. Also given in Table II are the lattice constants obtained for the lowest energy structure of $Li_7P_3O_{11}$.

Heat of formation energy results indicate that $Li_7P_3S_{11}$ is slightly stable relative to decomposition into its dimer and monomer components in the sense that

$$\Delta H(Li_7P_3S_{11}) - (\Delta H(Li_4P_2S_7) + \Delta H(Li_3PS_4)) = -0.1 \text{ eV}. \quad (3)$$

On the other hand from the relative stability of $Li_4P_2S_6$ and $Li_4P_2S_7$ indicated in Eq. (1), it is apparent that $Li_7P_3S_{11}$ is unstable with respect to decomposition into $Li_4P_2S_6$, Li_3PS_4, and S. In fact precipitation of $Li_4P_2S_6$ in the preparation of $Li_7P_3S_{11}$ has been reported.[4]

By contrast, $Li_7P_3O_{11}$ is unstable relative to decomposition into its dimer and monomer components in the sense that

$$\Delta H(Li_7P_3O_{11}) - (\Delta H(Li_4P_2O_7) + \Delta H(Li_3PO_4)) = 0.3 \text{ eV}. \quad (4)$$

The fact that $Li_7P_3O_{11}$ has not been reported in the literature is consistent with this analysis. However, we expect that $Li_7P_3O_{11}$ and its nitrided analogs may provide insight into possible local structures of the disordered electrolyte – LiPON.[6]

TABLE II: Lattice parameters for $Li_7P_3S_{11}$ and $Li_7P_3O_{11}$ determined by various experiments and simulations.

		a (Å)	b (Å)	c (Å)	α (Å)	β (Å)	γ (Å)
$Li_7P_3S_{11}$	(Exp.[2])	12.50	6.03	12.53	102.8^o	113.2^o	74.5^o
$Li_7P_3S_{11}$	(Exp.[36])	12.48	6.03	12.50	102.9^o	113.3^o	74.5^o
$Li_7P_3S_{11}$	(Cal. (USPP))	12.00	6.16	12.25	102.4^o	113.8^o	72.1^o
$Li_7P_3S_{11}$	(Cal. (PAW))	11.99	6.17	12.25	102.4^o	113.7^o	72.0^o
$Li_7P_3O_{11}$	(Cal. (USPP))	9.57	4.99	10.46	103.0^o	116.4^o	72.4^o
$Li_7P_3O_{11}$	(Cal. (PAW))	9.57	4.98	10.44	103.0^o	116.4^o	72.4^o

IV. Li ion migration analysis

In order to study Li ion migration in $Li_7P_3S_{11}$ we have considered both vacancy and interstitial mechanisms, using the nudged elastic band (NEB) method[12, 13, 14] to estimate barriers for migration between metastable defect sites. Because each metastable defect configuration involves a certain amount of distortion of the "host" lattice which contributes to migration energy barriers, it is useful to have a quantitative measure of this distortion. We can define a distortion parameter for each defect in the form

$$\mathcal{D}^{\rm Def}_{\rm atom} \equiv \frac{1}{N_{\rm atom}} \sum_{a \in {\rm atom}} |\mathbf{R}^a_{\rm Def} - \mathbf{R}^a_{\rm Ref}|. \quad (5)$$

This expression averages the distortion of each atom type separately. For each atom a of the "host" lattice, the distortion measures the displacement of the relaxed defect coordinate $\mathbf{R}^a_{\rm Def}$ compared with that of the perfect lattice $\mathbf{R}^a_{\rm Ref}$. $N_{\rm atom}$ denotes the number of atoms of a given type in the simulation cell.

a. Vacancy migration

Because of inversion symmetry, there are 7 inequivalent Li ion vacancy sites in each $Li_7P_3S_{11}$ unit cell. These are shown in Fig. 3. The relaxed vacancy structures were determined by using a fixed volume $1 \times 2 \times 1$ supercell. In order to approximate the electrically insulating properties of the electrolyte, an extra electron was added to the system and compensated by a uniform positive charge. While no attempt was made to correct for supercell errors,[37] we expect relative configuration energies to be well-approximated. The energies of the relaxed vacancy configurations relative to that of the most stable one (labeled **C**), as well as the distortion parameters defined in Eq. (5) are given in Table III.

Sites **A**, **D**, and **G** represent vacancies associated with the monomer (Li_3PS_4) groups and have similar energies. Sites **C**, **F**, **B** , and **E** represent vacancies associated with the dimer ($Li_4P_2S_7$) groups and the first 3 of those have lower energies than those associated with the monomer vacancies. The distortion parameters $\mathcal{D}^{\rm Vac}_{\rm atom}$ have no obvious correlation with the vacancy energies, but the values are similar for all of the configurations. We do observe that the P sites have the smallest distortion values, while the Li sites have the

greatest distortion values. The relatively small distortions of the P and S positions are presumably partially due to their covalent bonding.

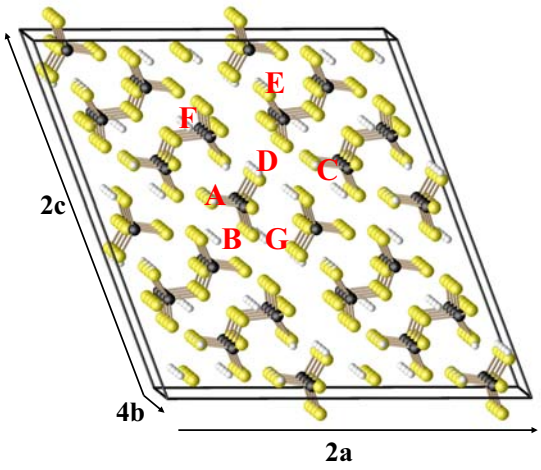

FIG. 3: Supercell of crystalline $Li_7P_3S_{11}$ indicating unique Li-vacancy sites.

TABLE III: Table of energies and distortions for unique vacancy sites in $Li_7P_3S_{11}$ calculated for a $1 \times 2 \times 1$ supercell. The vacancy labels are given in Fig. 3 and the energies are given relative to the most stable site (**C**). The distortion parameters are calculated using Eq. (5).

Label	E (eV)	$\mathcal{D}_{\mathrm{Li}}^{\mathrm{Vac}}$ (Å)	$\mathcal{D}_{\mathrm{P}}^{\mathrm{Vac}}$ (Å)	$\mathcal{D}_{\mathrm{S}}^{\mathrm{Vac}}$ (Å)
C	0.00	0.09	0.04	0.06
F	0.07	0.08	0.04	0.05
B	0.11	0.14	0.06	0.10
A	0.23	0.11	0.05	0.10
G	0.24	0.09	0.05	0.07
E	0.27	0.11	0.04	0.08
D	0.28	0.07	0.03	0.06

In order to investigate a vacancy mechanism for Li ion migration, we performed NEB calculations for hopping between various vacancy sites. These are shown in Figs. 4, 5, and 6. While additional paths for Li ion vacancy migration need to be investigated, the smallest migration barrier found so far for a through path is E_m=0.3 eV. The path corresponding to this E_m has net motion along the **b**-axis. Paths considered for net motion along the **a** and **c** axes have barriers of E_m=0.5 eV. Interestingly, in an earlier calculation for a metastable crystal of $Li_4P_2S_7$,[7] a minimal barrier for Li ion vacancy migration was found to be E_m

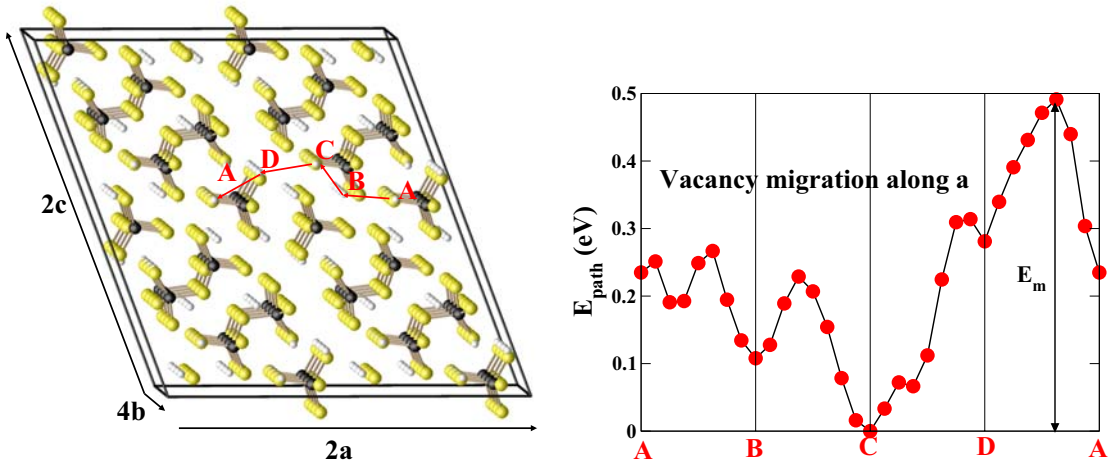

FIG. 4: Li ion vacancy diffusion in $Li_7P_3S_{11}$ along the **a**-axis.

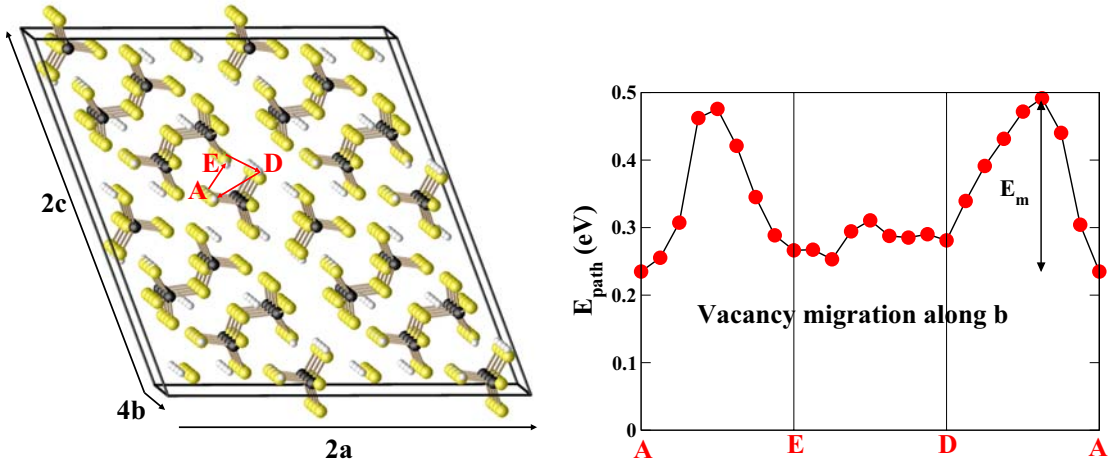

FIG. 5: Li ion vacancy diffusion in $Li_7P_3S_{11}$ along the **b**-axis.

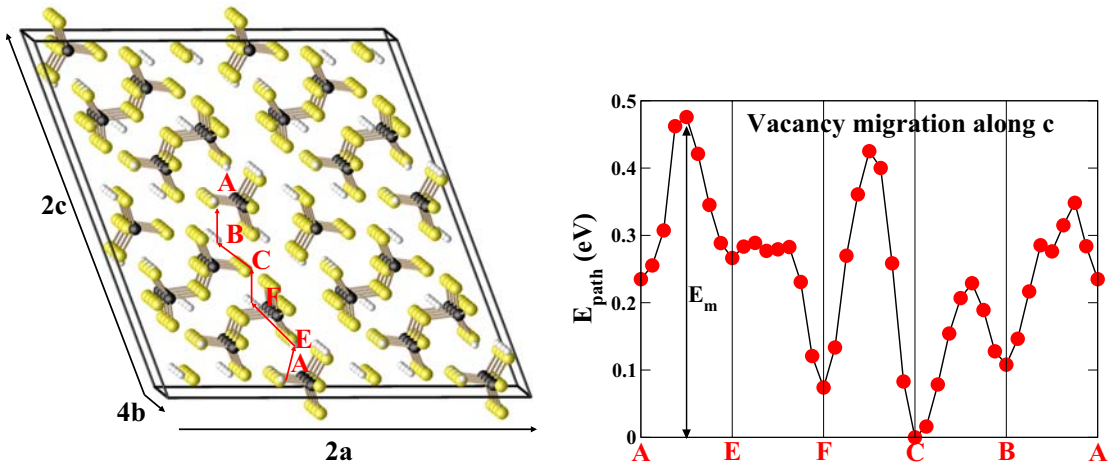

FIG. 6: Li ion vacancy diffusion in $Li_7P_3S_{11}$ along the **c**-axis.

≈ 0.3 eV.

b. Interstitial migration

The migration of interstitial Li ions was also considered. A grid of possible interstitial sites was constructed, the fineness of which was adjusted by making reasonable assumptions about the energy profile of this system. For each grid site, an interstitial Li ion was added to the perfect $1 \times 2 \times 1$ supercell and the system was allowed to relax at constant volume. As in the vacancy case, in order to approximate the electrically insulating properties of the electrolyte, an electron was removed from the system and compensated with a uniform negative charge. The lowest energy relaxed interstitial positions are visualized in Fig. 7 superposed on the perfect lattice supercell. These represent 6 non-equivalent positions, the most stable of which (α) is located at the origin of our supercell. The number of the meta-stable interstitial sites in close proximity appears promising for interstitial Li ion migration. Additionally, as shown below, the energy differences between these sites are small, a necessary condition for energetically favorable migrations between sites. This will be the subject of further work.

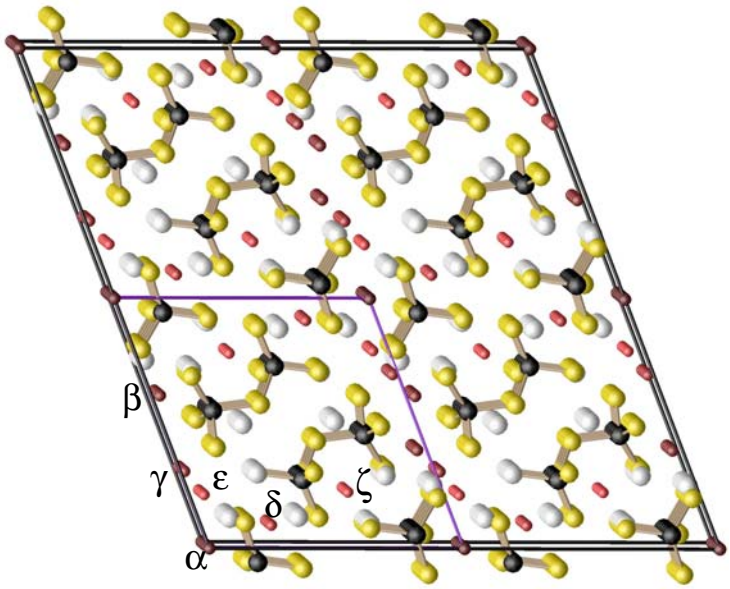

FIG. 7: Li ion interstitial sites visualized by superposition on the perfect $Li_7P_3S_{11}$ lattice. The interstitial sites are indicated with small dark red balls, using a dark to light variation to indicate the lowest to highest energy sites in the 0.00 - 0.19 eV energy scale. Inequivalent sites are labeled with Greek symbols.

While not shown in Fig. 7, in practice the interstitial Li ions cause significant distortions of the host lattice, especially among the neighboring Li ions. The host lattice distortion parameters $\mathcal{D}^{\rm Int}_{\rm atom}$ as well as the corresponding energies of the interstitial configurations (relative to the most stable configuration (α)) are given in Table IV. As in the case of the Li ion vacancies, we find that the P and S ions of the host lattice are relatively undistorted, while the host Li ions show appreciable rearrangements due to the interstitial ion. In general the distortions due to the interstitial Li ions shown in Table 7 are greater than those of the Li ion vacancies shown in Table 5. The value of $\mathcal{D}^{\rm Int}_{\rm Li}$ for the δ interstitial configuration reported in the Table is unusally large; several nearby host lattice Li sites are strongly perturbed in order to achieve the relaxed energy of 0.10 eV. In fact, with such large

TABLE IV: Relative energies and distortion measures of interstitial configurations in $Li_7P_3S_{11}$. For each of the low energy interstitial configuration labeled in Fig. 7 the energy E relative to the α configuration and the distortion lengths $\mathcal{D}^{\rm Int}_{\rm Li}$, $\mathcal{D}^{\rm Int}_{\rm P}$, and $\mathcal{D}^{\rm Int}_{\rm S}$ are given.

Label	E (eV)	$\mathcal{D}^{\rm Int}_{\rm Li}$ (Å)	$\mathcal{D}^{\rm Int}_{\rm P}$ (Å)	$\mathcal{D}^{\rm Int}_{\rm S}$ (Å)
α	0	0.24	0.05	0.08
β	0.07	0.13	0.06	0.08
γ	0.11	0.18	0.04	0.08
δ	0.11	0.49	0.10	0.18
ϵ	0.18	0.16	0.06	0.08
ζ	0.19	0.24	0.10	0.13

distortions, it is difficult to distinguish between interstitial and host lattice sites. In this case, we have found another interstitial configuration in the vicinity of the δ position with much smaller host lattice distortions but with substantially higher energy. This example gives some indication of the complicated nature of the energy profile of this material.

c. Vacancy-interstitial formation energies

During operation of a battery, there are generally sufficient sources of Li ion vacancies or interstitials so the migration process is dominated by the migration energy barriers E_m. However, for a perfect electrolyte crystal, the "formation" of these mobile defects is often the rate-limiting process. In general the formation process modifies the activation energy E_A for thermally activated conductivity according to

$$E_A = E_m + E_f/2. \tag{6}$$

By examining the energies of the various relaxed metastable vacancy-interstitial pair configurations relative to the energy of the perfect lattice preliminary results suggest that the minimum formation energy is less than $E_f \approx 0.1$ eV. Interestingly, this lowest energy vacancy-interstitial configuration involves the **C** vacancy site and α interstitial site. These correspond to the lowest energy vacancy configuration (most weakly bound host Li) and the lowest energy interstital configuration (most tightly bound interstitial Li) given in tables III and IV respectively. Comparison with our previous results[38] indicates that the vacancy-interstitial pair formation energy for $Li_7P_3S_{11}$ is substantially less than that of Li phosphate materials which are in the range $1.2 \leq E_f \leq 1.7$ eV.

VII. Summary and Conclusions

Our first principles simulations model a stable crystal phase of $Li_7P_3S_{11}$ as reported in the literature[2, 36] as well as a meta-stable phosphate analog – $Li_7P_3O_{11}$. For the

thiophosphate, the defect sites likely to be involved in Li-ion diffusion are studied in detail in preparation for modeling paths for ion conduction. For the vacancy mechanism, we have found several possible migration paths. The minimum migration barrier for the paths we have studied is found to be 0.3 eV, which provides an upper-bound on E_m for this material for the vacancy mechanism. So far, only pure vacancy mechanism migrations have been considered, though the high number of interstitial sites having relative energies between 0-0.2 eV indicates that they likely play a role in low-energy Li ion transport.

Experimental measurements of the activation energy for Li ion conductivity in $Li_7P_3S_{11}$ find $E_A \approx 0.12$ eV.[3] Our NEB results performed to date find larger activation energies than this experimental result. However our analysis of the interstitial configurations suggest that lower energy pathways involving interstitial or hybrid interstitial-vacancy mechanisms of Li ion migration may exist. This is the subject of ongoing investigations.

In addition, we are studying the migration barriers in corresponding phosphate and phosphonitride materials in order to understand the relationship between composition, structure, and ionic conductivity in these thiophosphate materials and LiPON-like solid electrolytes.

Acknowledgments

This work was supported by NSF grants DMR-0427055 and 0705239 and by the Wake Forest University DEAC computer cluster.

Bibliography

[1] F. Mizuno, A. Hayashi, K. Tadanaga, M. Tatsumisago, *Adv. Mater.* **17**, 918 (2005).

[2] H. Yamane, *et al.*, *Solid State Ionics* **178**, 1163 (2007).

[3] M. Tatsumisago, A. Hayashi, *Journal of Non-Crystalline Solids* **354**, 1411 (2008).

[4] K. Minami, A. Hayashi, M. Tatsumisago, *Journal of the Ceramic Society of Japan* **118**, 305 (2010).

[5] A. Hayashi, K. Minami, M. Tasumisago, *J. Solid State Electrochem.* **14**, 1761 (2010).

[6] N. J. Dudney, *Interface* **17**, 44 (2008).

[7] N. A. W. Holzwarth, N. D. Lepley, Y. A. Du, *Journal of Power Sources* **196**, 6870 (2011). http://dx.doi.org/10.1016/j.jpowsour.2010.08.042.

[8] P. Hohenberg, W. Kohn, *Physical Review* **136**, B864 (1964).

[9] W. Kohn, L. J. Sham, *Physical Review* **140**, A1133 (1965).

[10] P. Giannozzi, *et al.*, *J. Phys.: Condens. Matter* **21**, 394402 (19pp) (2009). Available from the website `http://www.quantum-espresso.org`.

[11] X. Gonze, *et al.*, *Computer Physics Communications* **180**, 2582 (2009). Code is available at the website `http://www.abinit.org`.

[12] H. Jónsson, G. Mills, K. W. Jacobsen, *Classical and Quantum Dynamics in Condensed Phase Simulations*, B. J. Berne, G. Ciccotti, D. F. Coker, eds. (World Scientific, Singapore, 1998), pp. 385–404.

[13] G. Henkelman, B. P. Uberuaga, H. Jónsson, *J. Chem. Phys.* **113**, 9901 (2000).

[14] G. Henkelman, H. Jónsson, *J. Chem. Phys.* **113**, 9978 (2000).

[15] OpenDX – The Open Source Software Project Based on IBM's Visualization Data Explorer – is available from the web site `http://www.opendx.org`.

[16] A. Kokalj, *Journal of Molecular Graphics and Modelling* **17**, 176 (1999).

[17] Y. A. Du, N. A. W. Holzwarth, *Phys. Rev. B* **81**, 184106 (15pp) (2010). Http://link.aps.org/doi/10.1103/PhysRevB.81.184106.

[18] D. Vanderbilt, *Phys. Rev. B* **41**, 7892 (1990). USPP code is available from the website `http://www.physics.rutgers.edu/~dhv/uspp/`.

[19] P. E. Blöchl, *Phys. Rev. B* **50**, 17953 (1994).

[20] N. A. W. Holzwarth, A. R. Tackett, G. E. Matthews, *Computer Physics Communications* **135**, 329 (2001). Available from the website `http://pwpaw.wfu.edu`.

[21] H. J. Monkhorst, J. D. Pack, *Phys. Rev. B* **13**, 5188 (1976).

[22] B. N. Mavrin, V. V. Asonov, V. V. Fomichev, A. K. Ivanov-Shitz, V. V. Kireev, *Journal of Experimental and Theoretical Physics* **96**, 53 (2003).

[23] F. Harbach, F. Fischer, *Phys. Stat. Sol. (b)* **66**, 237 (1974).

[24] L. Popović, B. Manoun, D. de Wall, M. K. Nieuwoudt, J. D. Comins, *Journal of Raman Spectroscopy* **34**, 77 (2003). Numerical values of the frequencies reported in this paper were obtained by manually digitizing the unlabeled peaks.

[25] Y. A. Du, N. A. W. Holzwarth, *Phys. Rev. B* **76**, 174302/1 (2007).

[26] J. P. Perdew, Y. Wang, *Phys. Rev. B* **45**, 13244 (1992).

[27] J. P. Perdew, K. Burke, M. Ernzerhof, *Phys. Rev. Lett.* **77**, 3865 (1996). Erratum – Phys. Rev. Let. **78**, 1396 (1997).

[28] D. R. Lide, ed., *CRC Handbook of Chemistry and Physics, 90th Edition* (CRC Press, Taylor & Francis Group, 2009). ISBN 13: 978-1-4200-9084-0.

[29] L. G. Cota, P. de la Mora, *Acta Cryst. B* **61**, 133 (2005).

[30] W. S. McDonald, D. W. J. Cruickshank, *Acta Cryst.* **22**, 48 (1966).

[31] A. G. Nord, *Acta Cryst. B* **32**, 982 (1976).

[32] T. Hahn, ed., *International Tables for Crystallography, Volume A: Space-group symmetry, Fifth revised edition* (Kluwer, 2002). ISBN 0-7923-6590-9. The symmetry labels used in this work are all based on this reference.

[33] R. Mercier, J. P. Malugani, B. Fays, J. Douglade, G. Robert, *Journal of Solid State Chemistry* **43**, 151 (1982).

[34] J. Schmedt auf der Günne, H. Eckert, *Chem. Eur. J.* **4**, 1762 (1998).

[35] A. Daidouh, M. L. Veiga, C. Pico, M. Martinez-Ripoll, *Acta Cryst. C* **53**, 167 (1997).

[36] Y. Onodera, *et al.*, *J. Phys. Soc. Jpn.* **79**, 87 (2010). Suppl. A; Proc. 3rd Int. Conf. Physics of Solid State Ionics (ICPSSI-3).

[37] G. Makov, M. C. Payne, *Phys. Rev. B* **51**, 4014 (1995).

[38] Y. A. Du, N. A. W. Holzwarth, *ECS Trans.* **25**, 27 (2010).